On the role of microstructure in governing the fatigue behaviour of nanostructured bainitic steels

Rosalia Rementeria[a], Lucia Morales-Rivas[a], Matthias Kuntz[b], Carlos Garcia-Mateo[a], Eberhard Kerscher[c], Thomas Sourmail[d], Francisca G. Caballero[a].
[a]Department of Physical Metallurgy, Spanish National Center for Metallurgical Research (CENIM-CSIC), Avda. Gregorio del Amo 8, E-28040 Madrid, Spain, rosalia.rementeria@cenim.csic.es, lucia.morales@cenim.csic.es, cgm@cenim.csic.es, fgc@cenim.csic.es
[b]Robert Bosch GmbH, Materials and Processing Dept, Renningen, 70465, Stuttgart, Germany, matthias.kuntz2@de.bosch.com
[c]University of Kaiserslautern, Materials Testing, Gottlieb-Damiler-Straße, 67663 Kaiserslautern, Germany, kerscher@mv.uni-kl.de
[d]Ascometal-CREAS (Research Centre) Metallurgy, BP 70045, Hagondange Cedex 57301, France, thomas.sourmail@ascometal.com

Corresponding Author:
F.G. Caballero
Spanish National Center for Metallurgical Research (CENIM-CSIC)
Av. Gregorio del Amo, 8
28040 MADRID
Spain

Tlf: +34 91 553 89 00 (Ext 373)
Fax +34 91 534 7425
E-mail: fgc@cenim.csic.es

Abstract

Nanostructured bainite is not a novel laboratory-scale steel anymore and the interest on the commercial production of these microstructures by steelmakers and end-users is now conceivable. These microstructures are achieved through the isothermal transformation of high-carbon high-silicon steels at low temperature, leading to nanoscale plates of ferrite with thickness of 20–40 nm and retained austenite. Nanostructured bainitic steels present the highest strength/toughness combinations ever recorded in bainitic steels (2.2 GPa/40 MPa·$m^{1/2}$) and the potential for engineering components is alluring. However, fatigue properties, responsible of the durability of a component, remain to be examined. In order to understand the role of the microstructure during the fatigue crack propagation, the crack path in three nanoscale bainitic structures has been analysed on the basis of the relationships between grain misorientations and grain boundaries by Electron Backscatter Diffraction. Active slip systems in bainitic ferrite and crack deflection at grain boundaries have been identified, while retained austenite is cast doubt on its role.

Keywords: bainite, fatigue, EBSD, steel

Introduction

Since the development of nanostructured bainitic steels [1-5], steel makers, end-users and scientists have devoted great attention and efforts to understanding both the transformation mechanism [6-15] and the origin of their outstanding mechanical properties [16-24] towards their industrialization [25]. It is well established that the nanoscale ferritic plates achieved through slow transformation at very low temperatures are responsible for strengthening up to levels of 2.2 GPa with a hardness of about 700 HV

[5]. These plates of bainitic ferrite are dispersed in carbon-enriched regions of retained austenite, which is assumed to be determining for ductility [21, 24, 26], though the deformation mechanisms responsible for such an advantageous combination of properties are the subject of ongoing discussions.

Nonetheless, most applications of structural materials involve cyclic loading and life of a component is generally limited by fatigue and not by static strength. In order to fully exploit the potential of nanostructured bainitic steels in industrial applications, a better understanding must be achieved on the relationship between microstructure and in-service properties.

As of today, little work has been published on nanostructured bainite fatigue properties. Peet et al. were the first authors on reporting fatigue tests on these steels [27]; with a stress ratio R=0.1 they set the maximum number of cycles on 10^5 and extrapolated the results up to 10^7 cycles to estimate the fatigue strength. The validity of this method is undermined when considering the anomalous two-stepwise or duplex S–N curves observed in high-strength steels [28-33]. Later results on high-cycle bending fatigue on nanostructured bainitic steels [34] revealed that the fatigue limit for no failure in 10^7 cycles is determined not only by hardness or strength but also by microstructure, so that retained austenite and secondary cracks in fatigue fractures have positive effects on the fatigue resistance. Latest work of Leiro et al [35] comparing the rotating bending fatigue behaviour of Quenched and Tempered (QT) and nanobainitic steels, showed an increase in fatigue properties of the latter mainly as a result of the refinement of the microstructure, the suppression of carbide precipitation and the Transformation Induced Plasticity (TRIP) effect. Regarding the latter, the benefits of the retained austenite in the fatigue performance of bainitic steels have been thoroughly discussed [27, 34, 36]. It has been found that the presence of retained austenite increases the threshold intensity [36], and its stress or strain induced transformation to martensite can blunt the crack by absorbing more energy than necessary for fatigue crack propagation [34].

On the other hand, many engineering components contain a variety of stress concentrators such as grooves, fillets, holes, or non-metallic inclusions. It has been observed that fatigue failure usually occurs as a result of crack initiation and growth from these stress raisers. Then, correct estimations of stress/strain concentration and crack development in the critical region are essential for practical machine design in service loading. Hence, in this work notched tension-tension fatigue will be explored in order to study the behaviour of nanostructured bainitic microstructures for actual engineering applications.

The fatigue limit of most metallic materials, for both notched and un-notched bodies, is determined by the propagation condition of nucleated small cracks. The crack closure and microstructural barriers are the two mechanisms for blocking small crack propagation at the fatigue limit [37]. Microstructural barriers in bainitic steels come from the nature of the displacive transformation itself, where it is generally assumed that close-packed {111} plane of the austenite (face-centred cubic, FCC) is exactly parallel to a {110} plane of the bainitic ferrite (body-centered cubic, BCC). In nanobainitic steels, most of the bainitic plates and the parent austenite interfaces are found to have an orientation relationships (OR) close to the Nishiyama–Wassermann (N-W), $\{111\}\gamma||\{110\}\alpha$ with $<110>\gamma||<001>\alpha$ [38, 39]. The transformed products, however, possess the lattice invariant line rather than the plane and direction parallelism between bainitic ferrite and parent austenite. Therefore, the relative orientation can never be precisely the N-W, and it may alter between Kurdjumov-Sachs (K-S) and N-W depending in the ratio of the lattice parameters between the parent austenite and bainitic ferrite [40]. From a single austenite crystal, 12 crystallographic variants can be formed with a N–W orientation relationship due to the

symmetry of cubic systems. A crystallographic packet is defined as a group of crystallographic variants with common {111} austenite plane (i.e. the same habit plane). Each bainite packet can be divided into bainite blocks of the three variants of the N–W relationship satisfying the same parallel plane relationship [41]. In consequence, the microstructure obtained is highly misoriented featuring a wide variety of potential microstructural barriers.

This work will analyze the fatigue crack propagation in nanostructured bainitic steels on the basis of its deflection due to the crystallographic orientation and boundary distribution. The main goal is to understand the role of both ferrite and austenite crystals on crack transmission and deflection across boundaries, and how this finally has an effect on fatigue life.

Materials and experimental procedure

The chemical compositions of the alloys investigated are 0.67C-1.67Si-1.31Mn-0.20Ni-1.73Cr-0.15Mo-0.18Cu-0.03Al-0.12V and 0.99C-2.47Si-0.74Mn-0.12Ni-0.97Cr-0.03Mo-0.17Cu-0.02Al wt. %, encoded as 0.6CV and 1CSi, respectively. Heats were industrially manufactured via electric arc furnaces. Once solidified, the ingots were reheated to 1200 °C and hot rolled to 120 mm diameter bars for 0.6CV steel and to 35 mm bars for 1CSi steel, which were afterwards slowly cooled down in a furnace to avoid cracking. After cooling, the bars were annealed for 2 h at 690 or 700 °C to further soften the material and ease machining of mechanical testing specimens.

Tensile and fatigue specimens were pre-machined after annealing to within 0.3 mm of the final dimensions and then austenitized. Austenitization conditions were selected in a way to obtain the same prior austenite grain size in all the specimens. The following three different nanobainitic microstructures were obtained after subsequent isothermal treatments: 0.6CV at 250 °C during 10 h, 0.6CV/250; 0.6CV at 270 °C during 7 h, 0.6CV/270; and 1CSi at 250 °C during 16 h, 1CSi/250. After transformation, the specimens were hard machined to the final dimensions under identical conditions to achieve similar surface roughness.

Tensile tests were conducted at room temperature and a strain rate of 0.004 s^{-1} with round tensile specimen with a gauge diameter of 8 mm and gauge length of 20 mm.

Notched conditions selected for fatigue testing are representative of the functioning of heavily loaded diesel injection components. The geometry of the notched specimen is shown in Figure 1. Fatigue tests were carried out in a pulsating machine following the Up-and-Down strategy [42] at a stress ratio (R) of 0.1 and a loading frequency of 150 Hz. Fatigue strength for a probability of failure of 50% (mean value) at 10^7 cycles was calculated according to the Probit method [42]. Failure mechanisms were distinguished by Scanning Electron Microscopy (SEM) examination of the fracture surfaces after testing. Microstructure below the fatigue fracture surface was examined by Field Emission Gun - Scanning Electron Microscopy (FEG-SEM) and Electron Backscatter Diffraction (EBSD) on nickel-plated cross sections of fracture surfaces cut through the crack initiation point on samples for 0.6CV/250 and 0.6/270 and 1CSi/250.

Samples for metallographic observation, both after fatigue testing and in the undeformed condition, were cut, ground and polished down to 2 μm diamond paste following the standard procedures. A 2% Nital etching solution was used to reveal the microstructure going over several cycles of etching and polishing to favour the etchant penetration, especially relevant for bainitic nanostructures. SEM observation was performed on a FEG-

SEM HITACHI S-4800 field emission gun scanning electron microscope, operating at 7 kV. In the case of the nanostructured bainite samples, high magnification FEG-SEM micrographs were used to determine the distribution and size of austenite blocks and coarse films, as well as the bainitic ferrite plate thickness, *t*, by measuring the mean lineal intercept $L_T=\pi t/2$ in a direction normal to the plate length[3, 43].

Quantitative XRD analysis was employed to determine the fraction of retained austenite and its lattice parameter for the estimation of the average carbon content in solid solution. For these experiments, samples were machined, ground and polished with 1 μm diamond paste, and then subjected to several cycles of etching and polishing to obtain an undeformed surface; finally the samples were polished with colloidal silica. X-ray diffraction measurements were performed by means of a Bruker AXS D8 diffractometer equipped with a Co X-ray tube and Goebel mirror optics to obtain a parallel and monochromatic X-ray beam. Operational parameters and the procedure for obtaining the austenite content and composition are described elsewhere [21, 44, 45].

Specimens for EBSD observations were carefully polished with 50 nm colloidal silica suspension at the final stage of metallographic preparation. EBSD analysis was performed by means of the HKL CHANNEL 5 system (Oxford Instruments) coupled to the FEG-SEM JEOL JSM 6500F microscope, operating at 20KV. A 16.5μm × 13.5μm area with a step size of 50 nm was scanned on undeformed samples. On fatigue specimens, a step size of 0.1 μm was maintained over an area of about 50 μm × 50 μm from the crack initiation point. It should be noted that the step size selected for the EBSD analysis is as large as the length of the smallest microstructural feature in these microstructures (the plate thickness), though for a representative data set a step size at approximately a tenth of the characteristic feature must be selected [46]. This parameter does not allow all the austenite nano-films to be indexed, so it must be kept in mind that these are omitted within the massive bainite blocks.

Results and discussion

FEG-SEM micrographs in Figure 2 show the bainitic structures obtained at low temperature in the three microstructures tested, consisting of bainitic ferrite plates (lower relief) and retained austenite (higher relief) as sub-micron blocks (100–1000 nm) and nano-films (<100 nm). Quantitative data on these microstructures are listed in Table 1. The main difference between the investigated microstructures is the austenite content, which is higher in 1CSi/250. On the other hand, the level of austenite carbon enrichment is higher in 0.6CV/270 than in 0.6CV/250. This appears at first in contradiction with the theory of bainite formation, whereby the retained austenite content is simply estimated by the lever rule as applied between ferrite and austenite of carbon content given by the T_0 line [47]. However, while this theory has been demonstrated to hold true at sufficiently high temperature [48-50], there is increasing evidence that at least part of the carbon remains trapped in ferrite and/or dislocations when transforming at lower temperatures [51-55]. Thus, it may be the case the higher carbon content of the austenite in 0.6CV/270 is a consequence of the lesser trapping at the higher transformation temperature when compared to 0.6CV/250.

Bainitic ferrite plate thickness measurements in Table 1 reveal that there is no further refinement in the microstructure of 0.6CV steel when the transformation temperature is lowered from 270 to 250 °C. However, a clear decrease in plate thickness is detected when the carbon content of the steel is increased, as revealed when comparing 0.6CV with 1CSi samples These results come to support and validate the theory that states that plastic relaxation in the austenite adjacent to the bainite plates controls the final size of the

bainitic ferrite plates [56]. The dislocation debris generated in this process resist the advance of the bainitic ferrite–austenite interface, the resistance being greatest for strong austenite.

Wöhler curves of 0.6CV/250 and 0.6CV/270 are shown in Figure3 (a) and (b), respectively, where the presence of two failure modes stands out: crack initiation from the surface and crack initiation from non-metallic inclusion beneath the surface. These two different failure modes divide fatigue behaviour in two regions within the S-N curves; early cracking (< 10^5 cycles) at higher stresses where crack initiation occurs at the surface, and later cracking (> 10^6 cycles) at slightly lower stress levels, where crack initiates on inclusions. These regions can be referred to as Low Cycle Fatigue (LCF) region for early cracking and High Cycle Fatigue (HCF) region for later cracking [57]. About the behaviour of these microstructures among both regions, 0.6CV/250 has a faintly better LCF behaviour (for a fixed stress amplitude under 10^5 cycles points are slightly displaced to higher endurances), whereas 0.6CV/270 shows faintly better HCF. However, these observations are not found to be statistically significant.

Fatigue results for 1CSi/250 in Figure 3 (c) are not as readily interpreted as those for 0.6CV. The division within two different failure modes is not as straightforward as in the case of 0.6CV. This material was found to have a higher amount of processing defects, i.e. non-metallic inclusions, and thus, part of the scatter in results can be explained by the initiations on inclusions. Nevertheless, the presence of inclusions cannot explain itself the comparably low fatigue resistance at the LCF regime of this microstructure.

Over the years, fatigue properties have been correlated to the monotonic tensile properties and hardness of the material [58-64]. Ductility has been found to predominate at short lives (LCF regime) while tensile and yield strength prevail at long lives (HCF regime), as high values of these retard fatigue crack nucleation. However, as yield strength is increased by the various strengthening mechanisms, the fatigue limit does not increase proportionately and most high-strength materials are fatigue limited. Monotonic tensile properties, fatigue strength at 10^7 cycles and hardness of the microstructures are listed in Table 2. In sight of the results, 1CSi/250 sample exhibiting the best combination of monotonic tensile properties has unexpectedly the poorest fatigue performance at both LCF and HCF regimes. Neither mechanical properties nor cleanliness of the alloy can explain this performance themselves, so a microstructural approach comes up necessarily.

For the investigation of the fatigue crack propagation mechanism, samples that went through early cracking with crack initiation at the surface were selected (highlighted in Figure 3). Fatigue crack growth process can be generally divided into the following three regions: slow expanding region, also called short (or small) crack propagation stage (Stage I); stable expanding region (Stage II); and rapid expanding region (Stage III) [65]. In the Stage I, the crack usually grows along the active slip bands immediately after its initiation, i. e. along slip planes in which the shear stress has maximum values, driven by the cyclic shear displacement at the crack tip.

Grain and phase boundaries may act as barriers against slip transmission into adjacent grains (depending on the orientation of the respective slip bands) and thus reduce the shear displacement at the crack tip exhibiting an oscillating growth [66, 67], decelerating the crack propagation [68]. Therefore, grain refinement is capable of increasing fatigue strength of the material by the insertion of a large quantity of microstructural barriers, i.e. grain boundaries, which have to be overcome in the stage I of propagation [68].

Active slip bands can be predicted by the resolved shear stress on the slip system as described by Schmid's law [69], which states that a crystalline solid flows plastically when

the resolved shear stress acting along the slip direction in the slip plane reaches a critical value, namely critical resolved shear stress. It is well known that in FCC structures, which have closed-packed {111} planes, the critical resolved shear stress is lower than in BCC crystal structures, which contain no closed packed-planes and a higher critical resolved shear stress must be exceeded before slip occurs. Therefore, crack propagation is expected to rely on the phase that needs higher stress to produce slip, BCC, assuming that the availability of active slip planes will be lower than for the FCC phase subjected to the same stress.

The theoretically activated slip planes were identified from EBSD data (represented in Figure 4 (a)) as those planes belonging to primary slip systems with maximum Schmid factor. Fig. 4 shows the crack path in a cross section perpendicular to the fracture surface. The crack started at the surface, which is on the left hand side, and grew from the upper left corner to the right hand side of the picture. Once identified the activated slip planes, slip traces were determined and then compared with the traces on the surfaces of the specimens. In Figure 4 (b) and (c), the correlation between theoretical active slip plane traces and the actual crack traces is shown for sample 0.6CV/270. These results show that the crack grows along the ferrite slip {110} <111> with the highest Schmid factor. The crack is significantly deflected at either ferrite/ferrite or ferrite/austenite boundaries between two different crystallographic bainite blocks. However, the crack is almost not deflected when encountering a ferrite/austenite boundary within a bainite block, implying that there is no change in the ferrite active slip plane after passing through that austenite. Thus, boundaries that are able to deflect the crack are those that delimit blocks, i.e., block boundaries, packet boundaries, twin austenite boundaries or prior austenite boundaries. Therefore, the microstructural feature controlling crack deflection, i.e., effective grain size, during the Stage I would be the bainite block size rather than the bainitic ferrite plate thickness. This does not necessarily mean that interphase boundaries within bainite blocks are not able to arrest the crack, but the extent of this arrestment would not be as effective as at deflecting boundaries.

EBSD analysis was performed in undeformed specimens, in order to determine the relationship between the fatigue resistance of the specimens and their crystallography. The crystallography was assessed by obtaining the bainite block size, as this parameter was found, in the previous analysis, to be relevant at the Stage I of crack propagation. The colours of the inverse pole figure (IPF) maps in Figure 5, selected to be representative of each microstructure, correspond to the crystallographic orientation normal to the observed plane, each colour representing a single crystallographic variant. The corresponding pole figures (PF) of a single prior austenite grain are also represented, reasserting that the OR in nanostructured bainitic steels resembles the N-W. The theoretical PF of the different OR can be found elsewhere [70]. These results show that the 0.6CV/250 sample has the finest bainite block size, while 0.6CV/270 and 1CSi/250 samples have coarser bainite blocks of comparable size. This supports previous observations in bainitic steels [71], whereby bainite blocks are refined by increasing the driving force (i.e. by lowering transformation temperature or carbon content).

According to Figure 3 and Figure 5, 0.6CV/250 and 0.6CV/270 present similar high fatigue strengths even though their bainite block sizes are quite different. On the other hand, 1CSi/250 shows the poorest fatigue performance having a large bainite block size, but its value being comparable to that of 0.6CV/270, with a higher fatigue strength. These results confirm that the effect of the grain size on fatigue behaviour is not that straightforward. In fact, experimental results obtained in micro-scale steels with grain sizes typically above 1μm [66, 72-75], show that in the Stage I of crack growth an increase in the grain size of the material generally results in a marked reduction in the Stage I fatigue crack growth rates and an increase in the threshold value for the propagation of long fatigue cracks

(ΔK_0), i.e. Stage II initiation. Moreover, it should be noted that the fatigue limit is a critical event both from the point of view not only of the crack propagation but also of the nucleation [76]. When considering low stacking fault energy materials, where the characteristic grain size has its greatest effect on fatigue life in the HCF regime in which Stage I cracking predominates over Stage II and III [77], fatigue life increases with decreasing grain size as it retards fatigue crack nucleation. The relative weight that the nucleation and the crack propagation stages have on the fatigue life might also vary between the materials studied. In addition, other microstructural parameters apart from the effective grain size should be playing an important role. For 0.6CV/270 and 1CSi/250 samples, with a comparable bainite block size, the higher amount of stable-austenite in 1CSi/250 may be contributing to crack nucleation in detriment of its fatigue life, perhaps by increasing the number of austenite-ferrite interphases where stress concentrates. On the other hand, the hardening effect of martensitic transformation during cyclic accommodation prior to crack nucleation is known to be beneficial for fatigue in fine-grained austenitic stainless steels [78]. It could be the case that austenite stability of 1CSi/250 microstructure does not lead to such a hardening behaviour during plastic accommodation as the less-stable austenite of 0.6CV microstructures, and fatigue resistance is thus reduced.

Conclusions

The fatigue behaviour of three different nano-bainitic structures has been analysed because macroscopic monotonic mechanical properties fail to explain it. A microstructural examination at the Stage I has shown that :

1. The crack deflects at the interphase boundaries between blocks, packets and twins of the ferritic phase, but not to a significant extent in the interphase boundaries within a single block.
2. The bainite block size is the crystallographic parameter controlling the crack propagation at this stage. However, its effect on the fatigue strength remains unclear, partially because it cannot be isolated from other microstructural features that are also likely to be affecting the mechanical behaviour.

Thus, even if a definitive conclusion cannot be drawn, fatigue behaviour of these steels is largely influenced by the microstructure. Main points of interest for further investigations are: (i) the TRIP behaviour of austenite during fatigue crack propagation as a function of its morphology (composition), (ii) favoured places for fatigue damage (crack initiation), and (iii) determination of the boundary strength and theoretical mechanism of crack propagation through ab-initio calculations coupled with molecular dynamics simulations.

Acknowledgements

The authors gratefully acknowledge the support of the Research Fund for Coal and Steel for funding this research under the Contract RFSR-CT- 2012-00017.

References

[1] F.G. Caballero, H.K.D.H. Bhadeshia, K.J.A. Mawella, D.G. Jones, P. Brown, Materials Science and Technology, 18 (2002) 279-284.
[2] C. Garcia-Mateo, F. Caballero, H. Bhadeshia, Journal De Physique Iv, 112 (2003) 285-288.
[3] C. Garcia-Mateo, F.G. Caballero, H.K.D.H. Bhadeshia, ISIJ International, 43 (2003) 1238-1243.
[4] C. Garcia-Mateo, F. Caballero, H. Bhadeshia, Revista De Metalurgia, 41 (2005) 186-193.
[5] C. Garcia-Mateo, F.G. Caballero, ISIJ International, 45 (2005) 1736-1740.
[6] D. Quidort, O. Bouaziz, Y. Brechet, in: E.B. Damm, M.J. Merwin (Eds.) Austenite Formation and Decomposition, Minerals, Metals & Materials Soc, Warrendale, 2003, pp. 15-25.
[7] L.C. Chang, Materials Science and Engineering: A, 368 (2004) 175-182.
[8] M. Takahashi, Current Opinion in Solid State and Materials Science, 8 (2004) 213-217.
[9] D. Gaude-Fugarolas, P.J. Jacques, ISIJ INTERNATIONAL, 46 (2006) 712-717.
[10] M. Jesus Santofimia, F.G. Caballero, C. Capdevila, C. Garcia-Mateo, C. Garcia de Andres, Materials Transactions, 47 (2006) 2473-2479.
[11] M. Jesus Santofimia, F.G. Caballero, C. Capdevila, C. Garcia-Mateo, C. Garcia de Andres, Materials Transactions, 47 (2006) 2465-2472.
[12] S.M.C. Van Bohemen, J. Sietsma, International Journal of Materials Research, 99 (2008) 739-747.
[13] I.A. Yakubtsov, G.R. Purdy, Metallurgical and Materials Transactions A: Physical Metallurgy and Materials Science, (2011) 1-10.
[14] M.J. Holzweissig, M.C. Uslu, H.G. Lambers, D. Canadinc, H.J. Maier, Materials Research Letters, 1 (2013) 141-147.
[15] T. Sourmail, V. Smanio, Acta Materialia, 61 (2013) 2639-2648.
[16] D. Liu, B. Bai, H. Fang, W. Zhang, J. Gu, K. Chang, Materials Science and Engineering A, 371 (2004) 40-44.
[17] C. Garcia-Mateo, F.G. Caballero, H.K.D.H. Bhadeshia, Mechanical properties of low-temperature bainite, Microalloying for New Steel Processes and Applications, Trans Tech Publications Ltd, Zurich-Uetikon, 2005, pp. 495-501.
[18] J.A.d.C. Junior, I.P. Pinheiro, T.F.M. Rodrigues, V.D.C. Viana, D.B. Santos, 18th IFHTSE Congress - International Federation for Heat Treatment and Surface Engineering, Rio Janeiro, 2010, pp. 4683-4691.
[19] M.Y. Matrosov, O.P. Talanov, I.V. Lyasotskii, D.L. Dyakonov, E.I. Khlusova, V.V. Orlov, A.M. Korchagin, D.S. Tsvetkov, S.D. Popova, Metallurgist, (2011) 1-9.
[20] J.A. Da Cruz Junior, T.F.M. Rodrigues, V.D.C. Viana, D.B. Santos, Bainite formation at low temperatures in high C-Si steel and its mechanical behavior, Quebec City, QC, 2012, pp. 173-180.
[21] B. Avishan, C. Garcia-Mateo, L. Morales-Rivas, S. Yazdani, F.G. Caballero, Journal of Materials Science, 48 (2013) 6121-6132.
[22] K. Zhu, O. Bouaziz, C. Oberbillig, M. Huang, Materials Science and Engineering A, 527 (2010) 6614-6619.
[23] Y. Wang, K. Zhang, Z. Guo, N. Chen, Y. Rong, Materials Science and Engineering: A, 552 (2012) 288-294.
[24] C. García-Mateo, F.G. Caballero, Materials Transactions, 46 (2005) 1839-1846.
[25] C. Garcia-Mateo, T. Sourmail, F.G. Caballero, V. Smanio, M. Kuntz, C. Ziegler, A. Leiro, E. Vuorinen, R. Elvira, T. Teeri, Materials Science and Technology, 30 (2014) 1071-1078.
[26] S.S. Babu, S. Vogel, C. Garcia-Mateo, B. Clausen, L. Morales-Rivas, F.G. Caballero, Scripta Materialia, 69 (2013) 777-780.
[27] M.J. Peet, P. Hill, M. Rawson, S. Wood, H.K.D.H. Bhadeshia, Materials Science and Technology, 27 (2011) 119-123.

[28] T. Sakai, M. Takeda, K. Shiozawa, Y. Ochi, M. Nakajima, T. Nakamura, N. Oguma, Zairyo/Journal of the Society of Materials Science, Japan, 49 (2000) 779-785.
[29] Y. Murakami, T. Nomoto, T. Ueda, Y. Murakami, Fatigue and Fracture of Engineering Materials and Structures, 23 (2000) 893-902.
[30] Y. Murakami, T. Nomoto, T. Ueda, Y. Murakami, Fatigue and Fracture of Engineering Materials and Structures, 23 (2000) 903-910.
[31] Y. Murakami, N.N. Yokoyama, J. Nagata, Fatigue and Fracture of Engineering Materials and Structures, 25 (2002) 735-746.
[32] K. Shiozawa, L. Lu, Fatigue and Fracture of Engineering Materials and Structures, 25 (2002) 813-822.
[33] T. Sakai, Y. Sato, N. Oguma, Fatigue and Fracture of Engineering Materials and Structures, 25 (2002) 765-773.
[34] J. Yang, T.S. Wang, B. Zhang, F.C. Zhang, Scripta Materialia, 66 (2012) 363-366.
[35] A. Leiro, E. Vuorinen, K.G. Sundin, B. Prakash, T. Sourmail, V. Smanio, F.G. Caballero, C. Garcia-Mateo, R. Elvira, Wear, 298–299 (2013) 42-47.
[36] L.I.U. Wenyan, Q.U. Jingxin, S. Hesheng, Journal of Materials Science, 32 (1997) 427-430.
[37] Y. Akiniwa, K. Tanaka, H. Kimura, Fatigue and Fracture of Engineering Materials and Structures, 24 (2001) 817-829.
[38] B.P.J. Sandvik, Metallurgical Transactions A, 13 (1982) 777-787.
[39] H. Beladi, Y. Adachi, I. Timokhina, P.D. Hodgson, Scripta Materialia, 60 (2009) 455-458.
[40] J.W. Christian, Metallurgical transactions. A, Physical metallurgy and materials science, 21 A (1990) 799-803.
[41] A.R. Marder, G. Krauss, Trans ASM, 60 (1967) 651-660.
[42] R.E. Little, Manual on Statistical Planning and Analysis for Fatigue Experiments, (1975).
[43] L.C. Chang, H.K.D.H. Bhadeshia, Materials Science and Technology, 11 (1995) 874-881.
[44] C. Garcia-Mateo, F.G. Caballero, M.K. Miller, J.A. Jimenez, Journal of Materials Science, 47 (2012) 1004-1010.
[45] D.J. Dyson, B. Holmes, Journal of the Iron and Steel Institute, 208 (1970) 469-474.
[46] A.J. Wilkinson, T.B. Britton, Materials Today, 15 (2012) 366-376.
[47] H.K.D.H. Bhadeshia, Bainite in Steels. Transformations, Microstructure and Properties, Second ed., Institute of Materials, Minerals and Mining, London, 2001.
[48] F.G. Caballero, M.J. Santofimia, C. Capdevila, C. García-Mateo, C. De García Andrés, ISIJ International, 46 (2006) 1479-1488.
[49] F.G. Caballero, M.K. Miller, C. Garcia-Mateo, C. Capdevila, C. Garcia de Andrés, JOM, 60 (2008) 16-21.
[50] F.G. Caballero, M.J. Santofimia, C. García-Mateo, J. Chao, C.G. de Andrés, Materials and Design, 30 (2009) 2077-2083.
[51] H.K.D.H. Bhadeshia, D.V. Edmonds, Acta Metallurgica, 28 (1980) 1265-1273.
[52] F.G. Caballero, M.K. Miller, S.S. Babu, C. Garcia-Mateo, Acta Materialia, 55 (2007) 381-390.
[53] A.J. Clarke, J.G. Speer, M.K. Miller, R.E. Hackenberg, D.V. Edmonds, D.K. Matlock, F.C. Rizzo, K.D. Clarke, E. De Moor, Acta Materalia, 56 (2008) 16-22.
[54] F.G. Caballero, M.K. Miller, C. Garcia-Mateo, Acta Materialia, 58 (2010) 2338-2343.
[55] F.G. Caballero, M.K. Miller, A.J. Clarke, C. Garcia-Mateo, Scripta Materialia, 63 (2010) 442-445.
[56] J. Cornide, C. Garcia-Mateo, C. Capdevila, F.G. Caballero, Journal of Alloys and Compounds, 577 (2013) S43-S47.
[57] S. Suresh, Fatigue of Materials, (1999).
[58] R.W. Landgraf, High Fatigue Resistance in Metals and Alloys, 1970.
[59] J.C. Grosskreutz, Metallurgical Transactions, 3 (1972) 1255-1262.
[60] C. Masuda, Y. Tanaka, Nippon Kikai Gakkai Ronbunshu, A Hen/Transactions of the Japan Society of Mechanical Engineers, Part A, 52 (1986) 847-852.
[61] J.-H. Park, J.-H. Song, International Journal of Fatigue, 17 (1995) 365-373.

[62] M.L. Roessle, A. Fatemi, International Journal of Fatigue, 22 (2000) 495-511.
[63] K.S. Kim, X. Chen, C. Han, H.W. Lee, International Journal of Fatigue, 24 (2002) 783-793.
[64] F.C. Campbell, Elements of Metallurgy and Engineering Alloys, (2008).
[65] S. Suresh, R. Ritchie, International Materials Reviews, 29 (1984) 445-475.
[66] S. Taira, K. Tanaka, M. Hoshina, ASTM Special Technical Publication, (1979) 135-173.
[67] K.J. Miller, Fatigue & Fracture of Engineering Materials & Structures, 10 (1987) 93-113.
[68] G. Totten, Advanced Materials and Processes, 166 (2008) 39-41.
[69] W. Read, Jnr, Acta Crystallographica, 4 (1951) 384.
[70] G. Nolze, Crystal Research and Technology, 41 (2006) 72-74.
[71] T. Furuhara, H. Kawata, S. Morito, G. Miyamoto, T. Maki, Metallurgical and Materials Transactions A: Physical Metallurgy and Materials Science, 39 A (2008) 1003-1013.
[72] J. Masounave, J.P. Baflon, Scripta Metallurgica, 10 (1976) 165-170.
[73] K. Tanaka, C. Masuda, S. Nishijima, 1981, pp. 450-460.
[74] A.K. Zurek, M.R. James, W.L. Morris, Metallurgical Transactions A, 14 (1983) 1697-1705.
[75] A. Järvenpää, L.P. Karjalainen, M. Jaskari, International Journal of Fatigue, (2013).
[76] P. Lukáš, M. Klesnil, Materials Science and Engineering, 34 (1978) 61-66.
[77] G.E. Dieter, Mechanical Metallurgy, (1986).
[78] A. Poulon, S. Brochet, J.-C. Glez, J.-D. Mithieux, J.-B. Vogt, Advanced Engineering Materials, 12 (2010) 1041-1046.

Figure captions

Figure 1: Notched geometry used for tension-tension fatigue tests

Figure 2: FEG-SEM micrographs of the undeformed microstructures for (a) 0.6CV / 250°C (b) 0.6CV / 270°C and (c) 1CSi / 250°C

Figure 3:Wöhler (*S-N*) curves of the specimens investigated: (a) 0.6CV / 250°C (b) 0.6CV / 270°C and (c) 1CSi / 250°C

Figure 4: Microstructure of the 0.6CV / 270 °C sample below the fracture surface: (a) ferrite Inverse Pole Figure (IPF) map showing crystallographic boundaries and corresponding Pole Figure (PF), where BB stands for Block Boundary, TB stands for twin boundary and PB stands for Packet Boundary, (b) corresponding FEG-SEM micrograph, and (c) calculated slip traces of the Stage I of crack propagation.

Figure 5: From left to right, EBSD Inverse Pole Figure (IPF) and Pole Figure (PF) maps of the undeformed specimens of (a) 0.6CV / 250 °C (b) 0.6CV / 270 °C and (c) 1CSi / 250 °C

Table captions

Table 1: Quantitative data on microstructures of metallographic samples

Table 2: Monotonic tensile properties, hardness and LCF life of the specimens studied

Table 1: Quantitative data on microstructures of metallographic samples

Sample	V_γ, %	C_γ, wt.%	V_α, %	α_b plate thickness, nm	$C_{\alpha b}$, wt.%
0.6CV / 250 °C	27±3	0.92±0.05	73±3	76±3	0.17±0.05
0.6CV / 270 °C	28±3	1.09±0.05	72±3	74±3	0.18±0.05
1CSi / 250 °C	40±3	1.18±0.05	60±3	32±1	0.21±0.05

V_γ, Volume fraction of retained austenite; C_γ, Average carbon content of the retained austenite; V_α, Volume fraction of bainitic ferrite; C_α, Average carbon content of bainitic ferrite;

Table 2: Monotonic tensile properties, hardness and LCF life of the specimens studied

Sample	0.2% Proof strength, MPa	Ultimate tensile strength, MPa	Uniform elongation, %	Total elongation, %	Hardness, HV30	Fatigue strength at 10^7 cycles
0.6CV / 250 °C	1490±19	2003±1	8.8±0.2	11.9±1.9	614±11	350
0.6CV / 270 °C	1287±19	1822±1	12.4±1.1	17.1±4.4	589±12	330
1CSi / 250 °C	1646±30	2072±1	11.7±0.2	16.4±2.2	658±14	245

Ø6 +0.01 -0.01
R1 +0.02 -0.02
Ø10 +0.02 -0.02

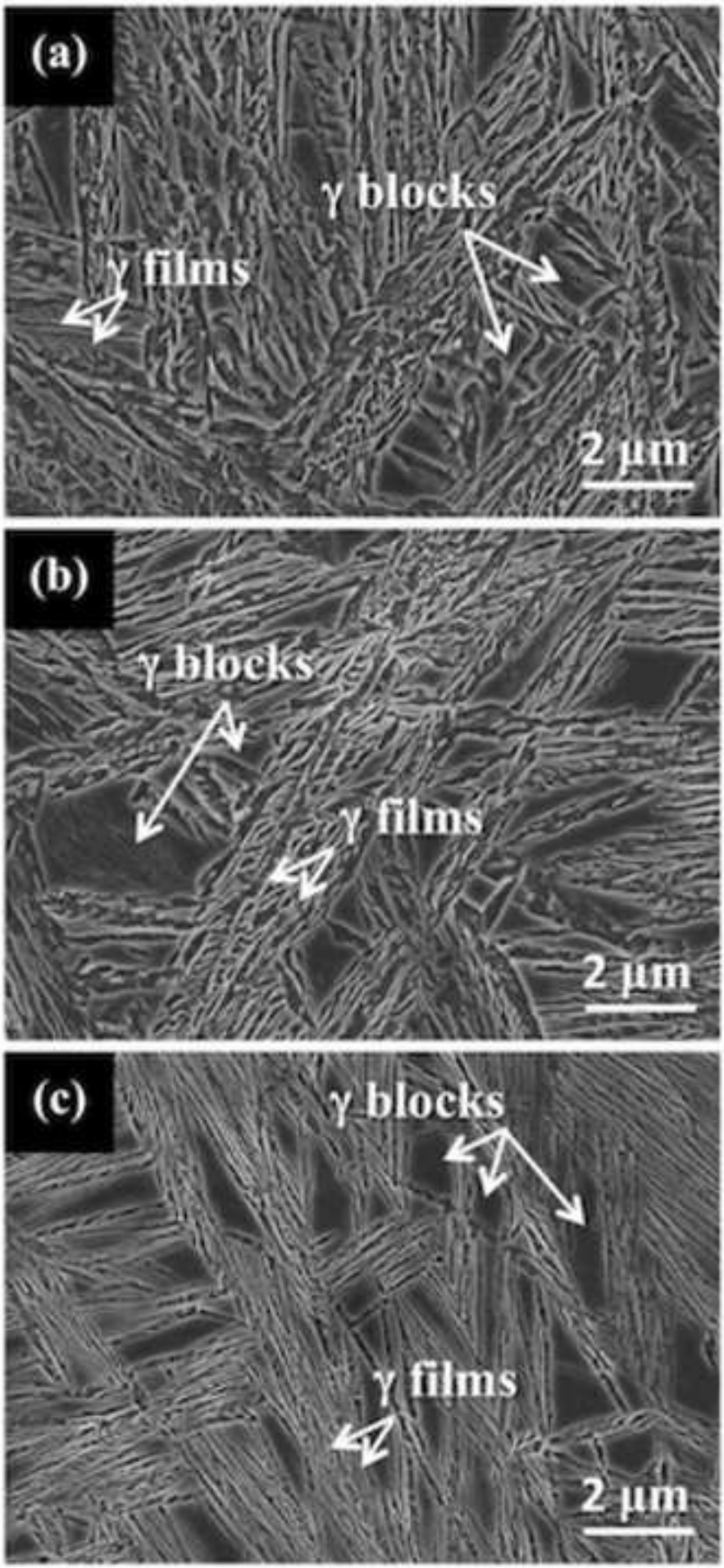
(a)
γ blocks
γ films
2 μm
(b)
γ blocks
γ films
2 μm
(c)
γ blocks
γ films
2 μm

(a)

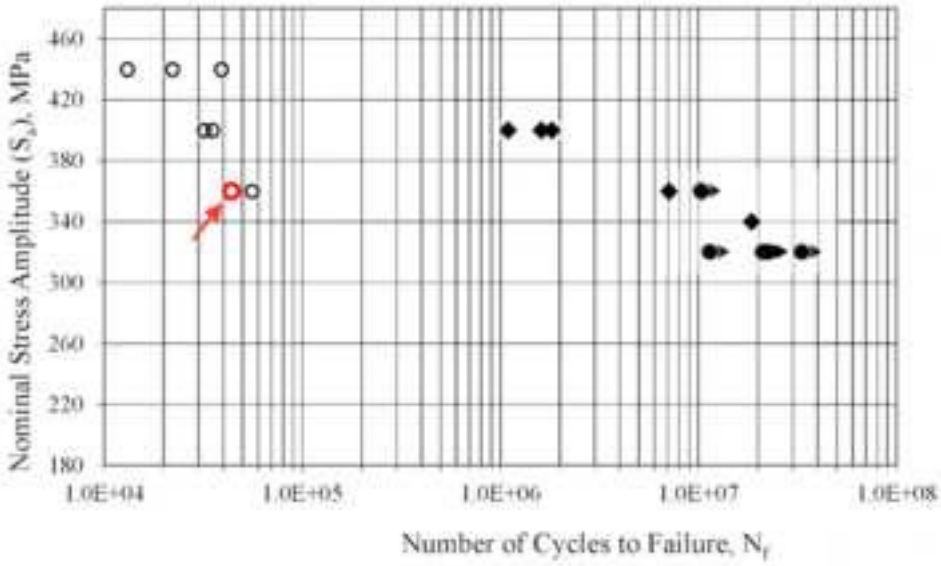
Nominal Stress Amplitude (S_a), MPa
460
420
380
340
300
260
220
180
1.0E+04
1.0E+05
1.0E+06
1.0E+07
1.0E+08
Number of Cycles to Failure, N_f

(b)

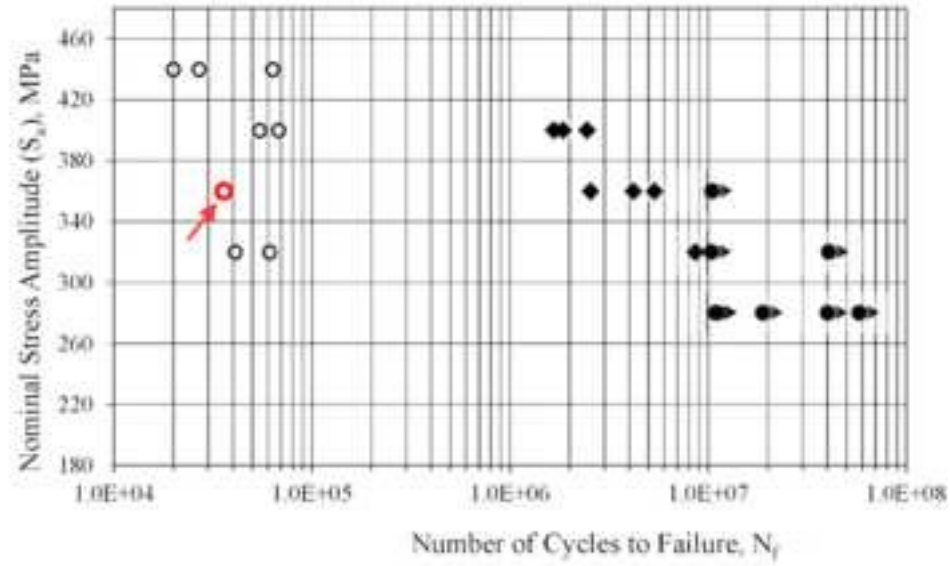
Nominal Stress Amplitude (S_a), MPa
460
420
380
340
300
260
220
180
1.0E+04
1.0E+05
1.0E+06
1.0E+07
1.0E+08
Number of Cycles to Failure, N_f

(c)

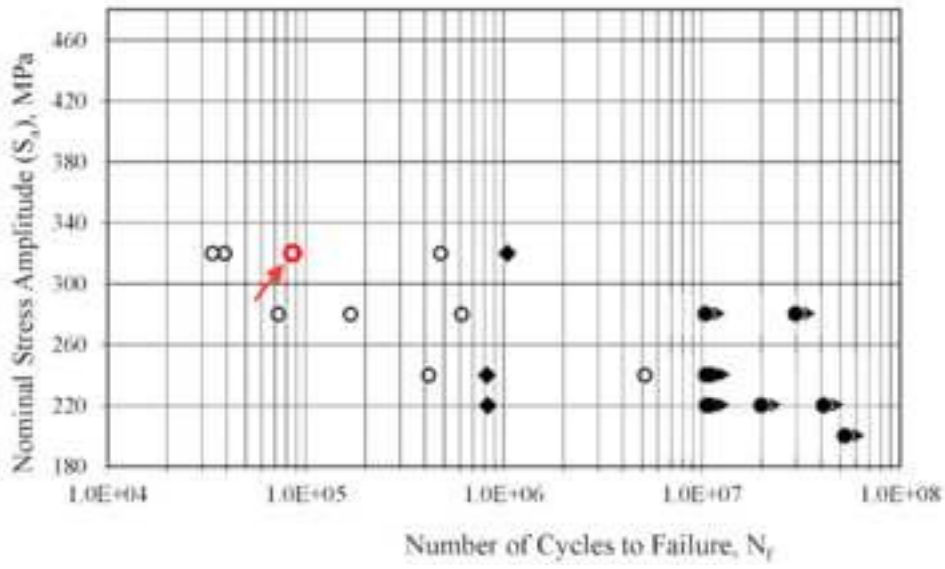
Nominal Stress Amplitude (S_a), MPa
460
420
380
340
300
260
220
180
1.0E+04
1.0E+05
1.0E+06
1.0E+07
1.0E+08
Number of Cycles to Failure, N_f

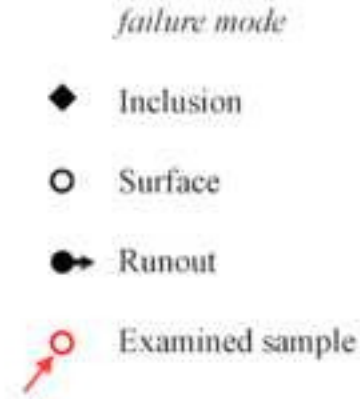
failure mode
Inclusion
Surface
Runout
Examined sample

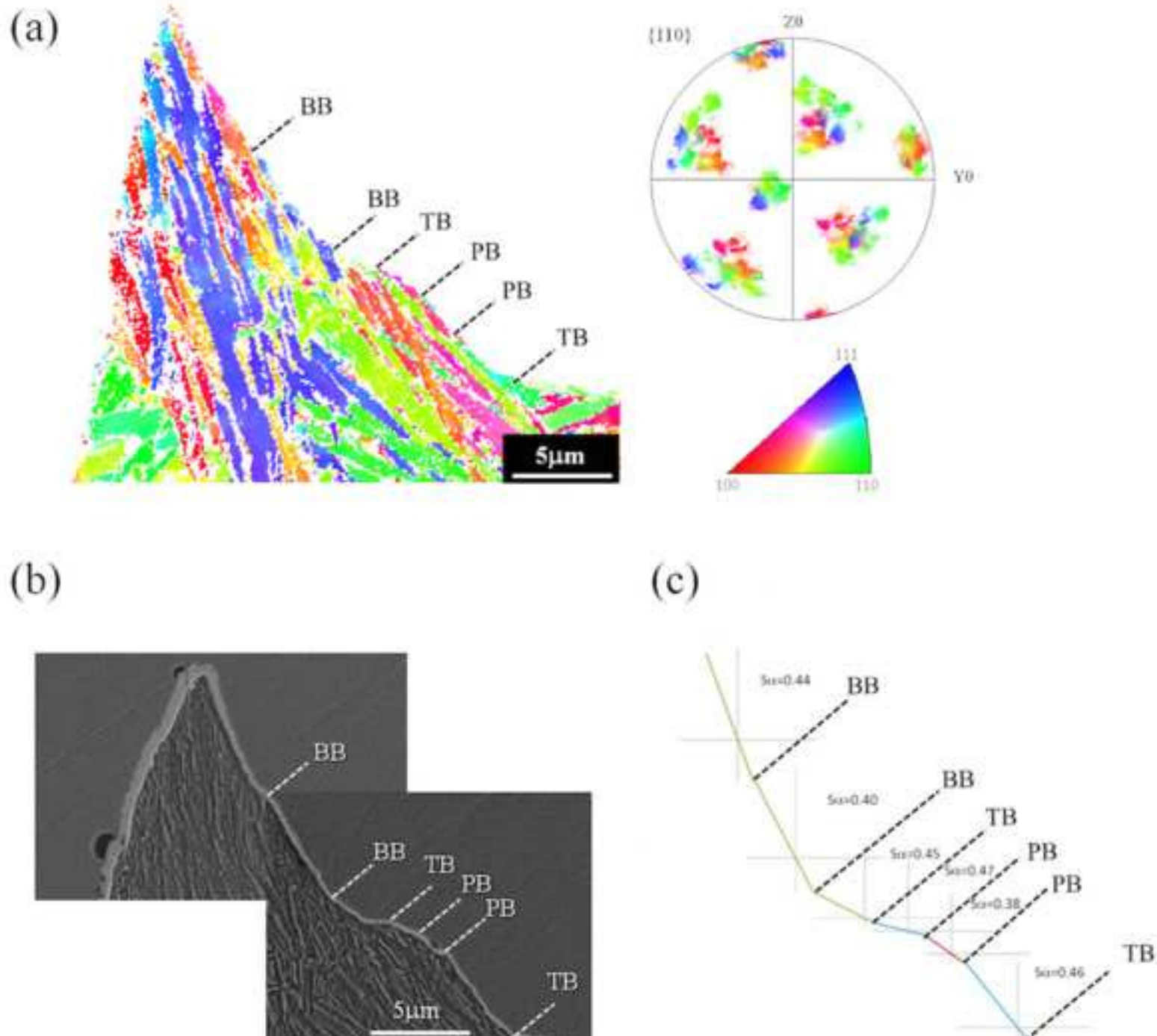
(a)
BB
BB
TB
PB
PB
TB
5μm
{110}
Z0
Y0
111
100
110
(b)
BB
BB
TB
PB
PB
TB
5μm
(c)
Sxx=0.44
BB
Sxx=0.40
BB
TB
Sxx=0.45
Sxx=0.47
PB
PB
Sxx=0.38
TB
Sxx=0.46

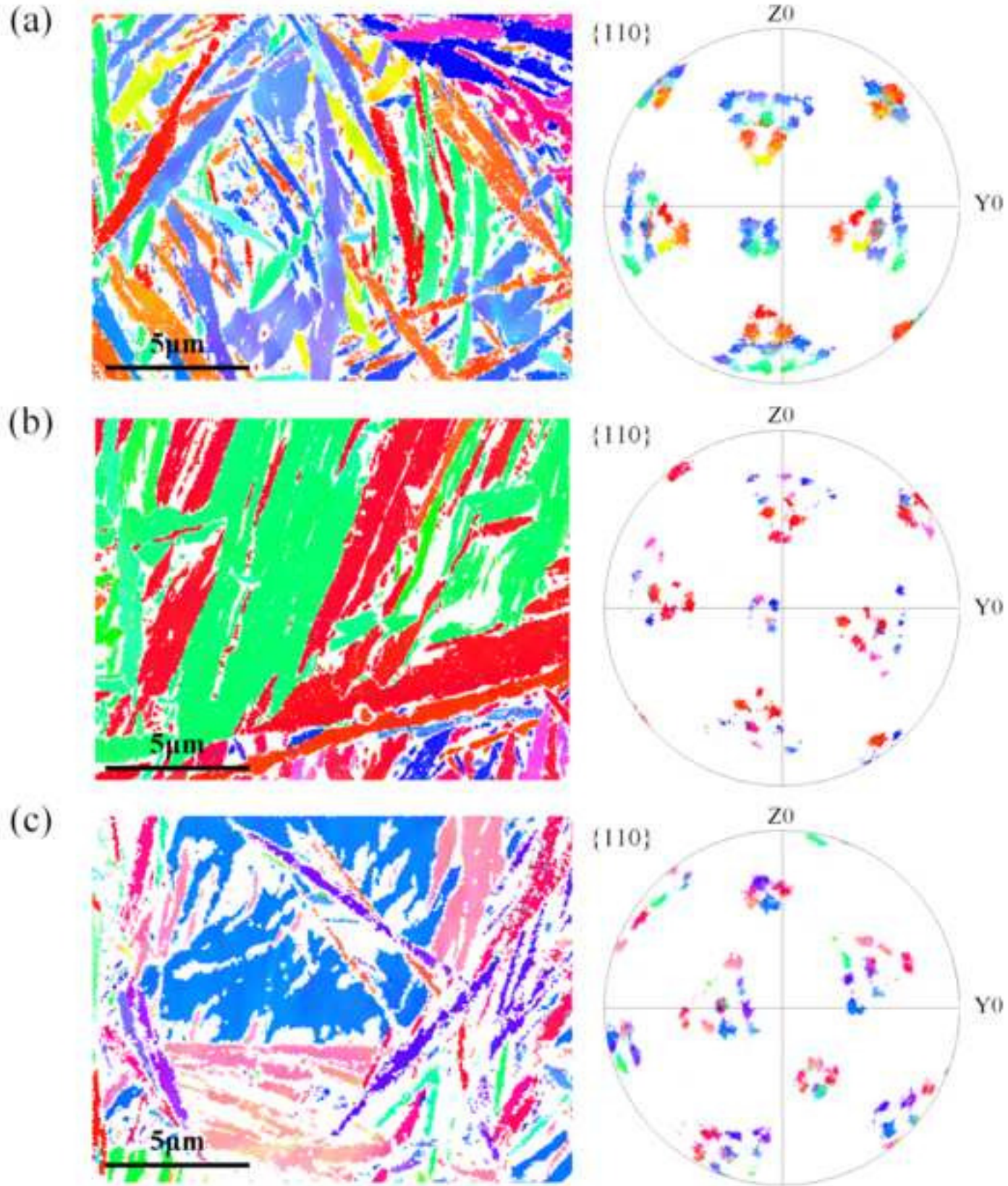
(a)
5μm
Z0
{110}
Y0
(b)
5μm
Z0
{110}
Y0
(c)
5μm
Z0
{110}
Y0